

Achieving Exceptional Strength-Ductility Synergy *via* Nano-precipitation Hardening in a Ni–Fe–Cr–Co–Al Alloy



SHUBHADA KAR, VIKAS SHIVAM, V.C. SRIVASTAVA, and G.K. MANDAL

In the present work, a Ni–Fe–Co–Cr–Al-based medium entropy alloy (MEA) was developed by exploring the vast compositional space provided by the birth of high-entropy alloys (HEAs). The composition was designed *via* the CALPHAD approach and the designed alloy was melted through the vacuum induction melting (VIM) technique using commercial elements. Post-homogenization treatment, the material was cold deformed up to 73 pct reduction in thickness. This cold-rolled material was annealed with varying duration at a fixed temperature of 900 °C for a better understanding of the static recrystallization mechanism. The systematic static recrystallization study was performed to design a heterogeneous grain distribution within the matrix *via* partial recrystallization. Post-establishment of the annealing schedule, ageing treatment at 600 °C for 5 hours was carried out. The room temperature mechanical properties were evaluated for selected ageing conditions. An excellent strength of > 950 MPa accompanied by an appreciable ductility of 60 pct was obtained for the fully recrystallized and aged specimen. The obtained results surpassed the strength-ductility synergy exhibited by various solid solution-strengthened (SS) Ni-based superalloys and heterogeneous HEAs and hold the potential to be explored for elevated temperature applications. A systematic study has also been carried out to estimate the contribution of various strengthening factors in the designed alloy and the predicted results corroborate well with the experimental findings.

<https://doi.org/10.1007/s11661-024-07402-y>

© The Minerals, Metals & Materials Society and ASM International 2024

I. INTRODUCTION

One of the major focus areas of materials scientists at present is the design and development of new alloys that are cost-competitive and possess unique combination of strength and ductility for various special applications including structural and aerospace sectors. The philosophy of design and development of novel alloys based on the equiatomic or near equiatomic multi-principal elements yielded high-entropy alloys (HEAs). This concept of high-entropy alloys (HEAs), as reported by Yeh *et al.*^[1] and Cantor *et al.*,^[2] demonstrated the stabilization of a single-phase random solid solution in multi-principal element alloys due to the dominance of mixing entropy of

the alloy system over mixing enthalpy. The single-phase random solid solution achieved in such complex alloy systems was explored further to achieve exceptional mechanical properties at room temperature,^[3–8] cryogenic,^[9,10] and high-temperature applications^[11,12] by tailoring the composition and final microstructure. Furthermore, alloy design for elevated temperature applications of such alloy systems was classified into two groups (a) refractory metal-based HEAs (RHEAs)^[13–16] and (b) transition metal-based HEAs (TM-HEAs).^[17–21] The RHEAs are generally comprised a disordered body-centred cubic (BCC_A1)-based matrix strengthened by ordered B2 precipitates (BCC_B2). The TM-HEAs were designed to obtain a microstructure consisting of ordered L1₂ (γ') precipitates in a disordered face-centred cubic (FCC) matrix (γ), as in the case of conventional superalloys. Moreover, these γ - γ' bearing TM-HEAs for elevated temperature applications were also known as high-entropy superalloys (HESAs).^[18,22] Early studies on HESAs exhibited better microstructural stability over conventional superalloys with suppression of the formation of various undesirable phases.^[18,22] However, later studies showed phase segregation and microstructural decomposition of several HESAs at elevated temperatures.^[20,23,24] Furthermore, the alloy design studies were not limited solely to high-entropy compositions and several medium entropy

SHUBHADA KAR is with the Academy of Scientific and Innovative Research (AcSIR), Ghaziabad 201002, India. Contact e-mail: shubhadakar93@gmail.com VIKAS SHIVAM is with the Materials Engineering Division, CSIR–National Metallurgical Laboratory, Jamshedpur 831007, India. V.C. SRIVASTAVA and G.K. MANDAL are with the Academy of Scientific and Innovative Research (AcSIR) and also with the Materials Engineering Division, CSIR–National Metallurgical Laboratory.

Manuscript submitted December 13, 2023; accepted April 3, 2024.

Article published online April 23, 2024

alloys (MEAs) were also explored.^[25–28] Many of the newly designed MEAs and HESAs exhibited excellent mechanical properties at both room and high temperatures.^[8,9,27,29] As a result, these γ - γ' bearing HESAs and MEAs are currently being considered as potential candidates as an alternative to superalloys for high-temperature applications.^[10,12,30] Further, the emergence of a promising strategy of heterogeneity engineering in HEAs^[6,31–33] has led to better strength-ductility synergy in these systems. Wang *et al.* designed a $\text{Co}_{23}\text{Cr}_{23}\text{Ni}_{23}\text{Mn}_{31}$ alloy and introduced a heterogeneous microstructure with the aid of rolling and annealing.^[4] The processing led to introduction of various nanoparticles, dislocations, nanotwins, stacking faults, Lomer-Cottrell locks, *etc.* which led to excellent strength-ductility synergy in the designed alloy. Sathiyamoorthi *et al.* reviewed various heterogeneous HEAs and the paradigm shift in the strength-ductility synergy was observed in these heterogeneous HEAs.^[34] They discussed the design of bimodal, lamellar, gradient and harmonic structures to improve the combination of strength and ductility. Gorsse *et al.* discussed the effectiveness of a hierarchical microstructure in attaining promising high-temperature yield strength in HESAs.^[35] Their work studied the kinetics of the γ - γ' phases and calculated the temperature-time-transformation (TTT) diagram to optimize the hierarchical microstructure in the HESAs.^[35] Recent works of Wang *et al.* designed hierarchical precipitates to harvest the benefit of heterogeneity engineering in improving the mechanical properties of the alloys.^[6] Hence, carefully designed cost-effective γ - γ' -based alloys with heterogeneous microstructures are potential candidates for wide temperature range applications and are currently under rigorous investigation.

In the present work, a novel low-alloyed medium entropy alloy (MEA) has been designed and engineered to obtain structural heterogeneity *via* partial recrystallization. The Ni–Fe–Co–Cr–Al alloy was designed using the CALPHAD approach and prepared through an induction melting and casting route. Post-homogenization treatment and a cold deformation of 73 pct, a set of systematic annealing experiments was performed by varying the annealing duration for comprehensive understanding of static recrystallization mechanism at a fixed annealing temperature of 900 °C. The main purpose of recrystallization study was to find out the suitable time-temperature schedule for heterogeneous microstructure design. A detailed microstructural characterization was carried out for both as-cast and thermo-mechanical processed specimens. Mechanical properties were evaluated at room temperature and compared with the existing literature of heterogeneous HEAs and solid solution (SS)-based superalloys. In addition, evaluation of various strengthening factors was carried out to assess their respective contribution for each processed condition in the designed alloy.

II. MATERIAL AND METHODS

A. Alloy Design and Preparation

The CALPHAD approach was adopted to design a suitable composition of $\text{Ni}_{49.5}\text{Fe}_{19.8}\text{Co}_{15}\text{Cr}_{12}\text{Al}_{3.7}$

system. The composition design aimed to mimic the γ - γ' microstructure of conventional superalloys *i.e.*, Ni_3Al (L_{12}) precipitates (γ') in a disordered face-centered cubic (FCC_A1) matrix (γ). The designed alloy was prepared through vacuum induction melting (VIM) and casting utilizing the commercial grade materials. The elemental materials with 98–99 pct purity (2 kg) were heated together in alumina (Al_2O_3) crucible up to 1600 °C and kept for 10 minutes for temperature and composition homogenization after completion of melting. The molten alloy was then poured into a copper mould of dimensions $41 \times 41 \times 180 \text{ mm}^3$. A specimen of dimensions $10 \times 10 \times 5 \text{ mm}^3$ was sectioned from the as-cast ingot and taken for chemical analysis. The chemical analysis was performed using the spark optical emission spectroscopy (Spark-OES) Gen-1 analysis technique and obtained results are mentioned in Table I.

A considerable amount of Fe was added with an objective to produce a low-cost and low-density alloy. Despite its high cost, Co was added in a significant amount taking into consideration its favorable influence on the recrystallization mechanisms and stacking-fault energy of the material.^[36] The presence of Al in the alloy promotes the formation of γ' phase and improves the corrosion resistance. The main purpose of Cr addition was to enhance the oxidation and corrosion resistance properties of the alloy. Further, Cr content in the alloy promotes the formation of Cr-based carbides, which might be beneficial for exploring its potential for high-temperature applications.^[37]

B. Thermo-mechanical Processing

The as-cast material of dimensions $38 \times 30 \times 25 \text{ mm}^3$ was kept at 1200 °C for 1 hours and hot forged up to 42 pct reduction in thickness and air cooled. The forged material was then cold-rolled up to 47 pct reduction in thickness and homogenized at 1050 °C for 1 hours. The homogenization treatment followed a similar processing route as our previous work which contained as-cast γ' precipitates and required heavy deformation for dissolution of as-cast precipitates to render a single-phase.^[8] A schematic representation of the detailed process schedule is shown in Figure 1.

The homogenized material was cold-rolled up to 73 pct thickness reduction to study the static recrystallization behavior of the material at 900 °C. The recrystallization study temperature of 900 °C was chosen based on our previous works performed on similar alloy systems.^[8] Small specimens with dimensions $3 \times 2.2 \times 1.6 \text{ mm}^3$ were annealed at 900 °C for varying durations of 20, 60, 120, 180, 300, 900 and 1800 seconds.

Post-establishment of the recrystallization kinetics of the designed alloy, based on theoretical and experimental studies, the cold-rolled specimen annealed at 900 °C for 900 seconds was taken for ageing treatment. Three specimens from the aforementioned annealed condition were selected and aged at 600 °C for 3, 5, and 8 hours. The evaluation of the average microhardness values of the studied specimens suggested that isothermal holding at 600 °C for 5 hours would be sufficient for suitable ageing for the chosen annealing condition.

C. Microstructural Characterization

Microstructural characterization of the specimens, processed under different conditions, was carried out on an optical microscope (OM), scanning electron microscope (SEM), and transmission electron microscope (TEM). Before investigation under OM, specimens were polished using SiC emery paper up to 2500 grit size followed by cloth polishing using alumina (Al_2O_3) of 1 μm size and colloidal silica. The specimens were then ultrasonically cleaned for 10 min using ethanol. and were etched using Waterless Kalling's reagent (2 g CuCl_2 , 40 mL HCl, and 40–80 mL ethanol). Optical micrographs were captured on a Leica DM2500M optical microscope. The analysis of microstructural features, including grain size, dendrite arm spacing and precipitate size, was performed using ImageJ 1.53e public domain software.

SEM study was performed on a Carl Zeiss instrument equipped with an Oxford EDS (energy dispersive spectroscopy) detector. A few selected specimens were evaluated for the distribution of strain and grain size using electron backscattered diffraction (EBSD) technique. The EBSD analysis was performed on a field emission gun (FEG)-SEM (Model- FEI Nova Nano) equipped with a TSL-OIM acquisition system and operating at 20 kV. The specimens were electropolished using a solution of 10 pct perchloric acid and 90 pct ethanol at 20 V. A step size of 0.5 μm was used for lower time step annealed specimens (60 and 120 seconds at 900 °C post 73 pct cold deformation) and 1 μm step size was chosen for specimen annealed for a longer duration of 300 and 900 seconds.

X-ray diffraction (XRD) analysis of the as-cast specimen was conducted on the Rigaku Ultima IV X-ray diffraction system (Cu- $\text{K}\alpha$ radiation with $\lambda = 0.154$ nm). The as-cast specimen was paper polished to 2500 grit, followed by diamond polishing. Specimen was scanned from 20 to 100 deg with a scan speed of 1°/min. The specimens processed as per chosen tensile test conditions were also scanned from 20 to 100

deg at 1°/min and analysed for determination of dislocation density. The XRD pattern analysis was carried out using X'Pert Highscore Plus (version 2.1) for the determination of plane spacing d , lattice parameter a and full width half maxima (FWHM).

Further, TEM characterization was carried out for the condition exhibiting the best combination of properties before and after the tensile tests *i.e.*, cold-rolled specimen annealed at 900 °C for 900 seconds, later aged at 600 °C for 5 hours. The specimens were cut using an electro-discharge machining (EDM) wire cutter and thinned down to 50 μm thickness. The thinned specimens of diameter 3 mm were punched from the sheet and subjected to twin jet polishing. A solution of 10 pct perchloric acid and 90 pct ethanol was used as the electrolyte with a current supply of 40 mA at -20 °C.

D. Mechanical Property Evaluation

The specimens for microhardness evaluation were paper polished to 2500 grit size followed by diamond polishing. The microhardness data were recorded on the cross-sectional plane parallel to the rolling direction using a Vickers Microhardness Tester (Omni-Tech-S. No. -551, Model F. Auto) at a load of 1000 g with a dwell time of 10 seconds. At least ten data points were collected to record the average hardness value for each condition.

Flat dog-bone-shaped specimens with a gauge length of 7.2 mm and gauge width of 3 mm were prepared for room temperature mechanical properties evaluation. The tensile tests were performed at a strain rate of 10^{-3} s^{-1} on Instron servo-electric universal testing machine (UTM). Before tensile tests, the specimens were paper polished to 1000 grit size to eliminate undesirable oxide scales and ensure a clean surface. Three specimens were tested for each chosen condition to ensure the reproducibility of the data.

Table I. Composition of Present Work (Wt Pct)

Composition	Ni	Fe	Co	Cr	Al
Chemical Analysis	bal.	19.8	15.5	12.0	3.7
Bulk-EDS	bal.	20.5	14.9	13.1	3.9

III. RESULTS

A. Alloy Design and Property Diagram

Figure 2 shows the property diagrams of the designed alloy predicted using the commercial thermodynamic

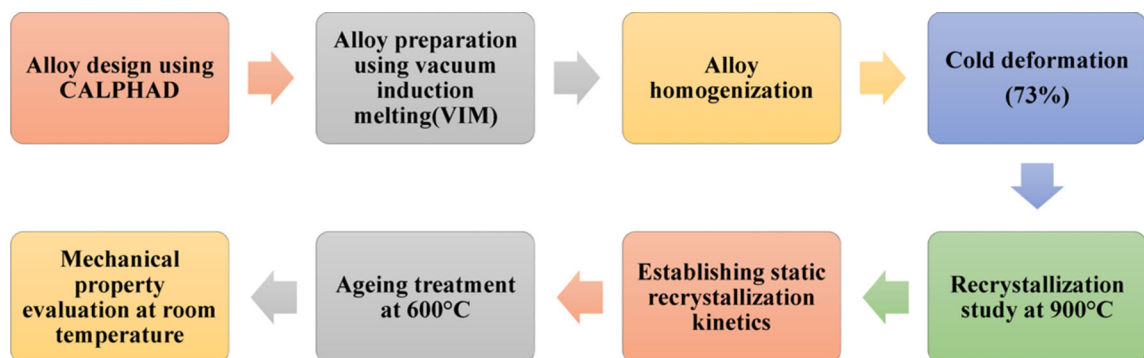


Fig. 1—Flow chart showing the process schedule followed in this study.

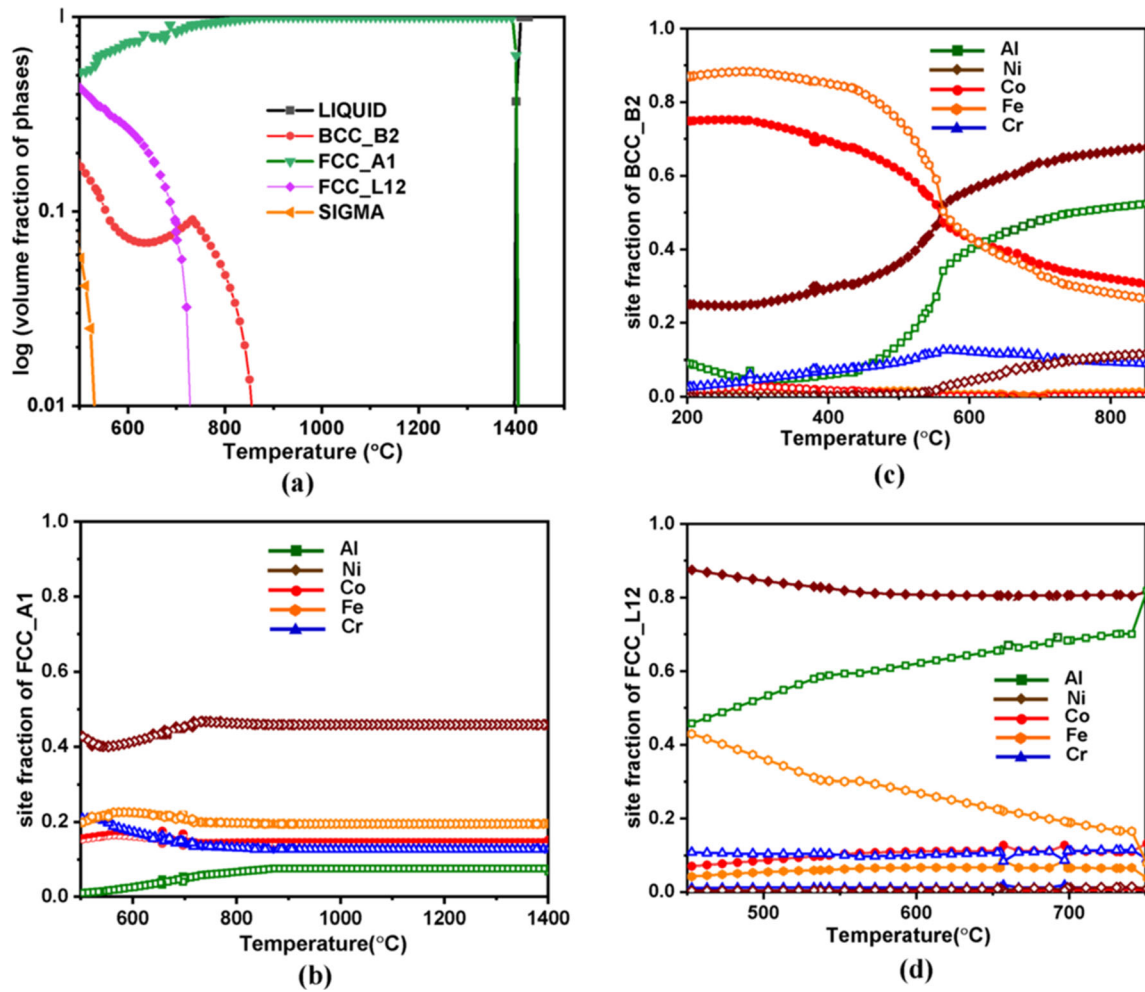


Fig. 2—(a) Property diagram of designed alloy, (b to d) site fraction of elements with respect to temperature for FCC_A1, BCC_B2 and FCC_L12 phase, respectively.

software package Thermo-Calc (2022b version) with the help of the TCHEA5 database.

Figure 2(a) shows the formation of a disordered FCC_A1 phase at around 1400 °C during equilibrium cooling of the liquid. The presence of a single-phase disordered FCC_A1 exists in the temperature range of 850 °C to 1380 °C. The precipitation of a BCC_B2 phase commences at 850 °C but the predicted volume fraction is quite low (< 10 pct). The precipitation of the ordered L1₂ phase (denoted as FCC_L12 in Figures 2(a) and (d)) is predicted to occur at ~ 720 °C and onset of sigma (σ) phase initiates at ~ 545 °C during equilibrium cooling of the alloy. The variation of site fraction of elements as a function of temperature, for each predicted phase (except σ), is shown in Figures 2(b) through (d). These property diagrams were calculated to assess the ordering and partitioning of the elements in various phases. The solid-filled shapes represent sublattice 1 and the hollow shapes denote sublattice 2 (Figures 2(b) through (d)). As both the lines (with solid fill and hollow shapes) merge for individual element as shown in Figure 2(b), a disordered matrix of FCC_A1 (γ) is confirmed. Figure 2(c) predicted onset of an ordered

BCC_B2 phase which is Ni and Al rich till 545 °C after which the phase gets Fe and Co rich at the lower temperatures. Figure 2(d) confirms the formation of an ordered FCC_L12 (γ') phase, where one sublattice is dominated by Ni atoms and another one enriched with Al atoms. It is also noted that the site fraction of one sublattice remains Ni-rich throughout the temperature range. Whereas, Al content in the second sublattice decreases with the enrichment of Fe with decrease in temperature. This Fe enrichment in second sublattice is more prominent below 545 °C due to the formation of sigma (σ) phase. This demonstrates the occupation of Al-sites by Fe at low temperature in FCC_L12 (γ') phase. Though thermodynamic analysis predicts the formation of BCC_B2 in the designed alloy system, the present work did not yield any ordered BCC_B2 precipitation. This can be attributed to the sluggish kinetics of formation of an ordered phase with very low volume fraction in the designed composition. The CALPHAD predicted Cr-rich σ phase is rarely realized in real alloy systems due to its complex structure. The predicted property diagrams clearly demonstrate the availability of a large temperature window for

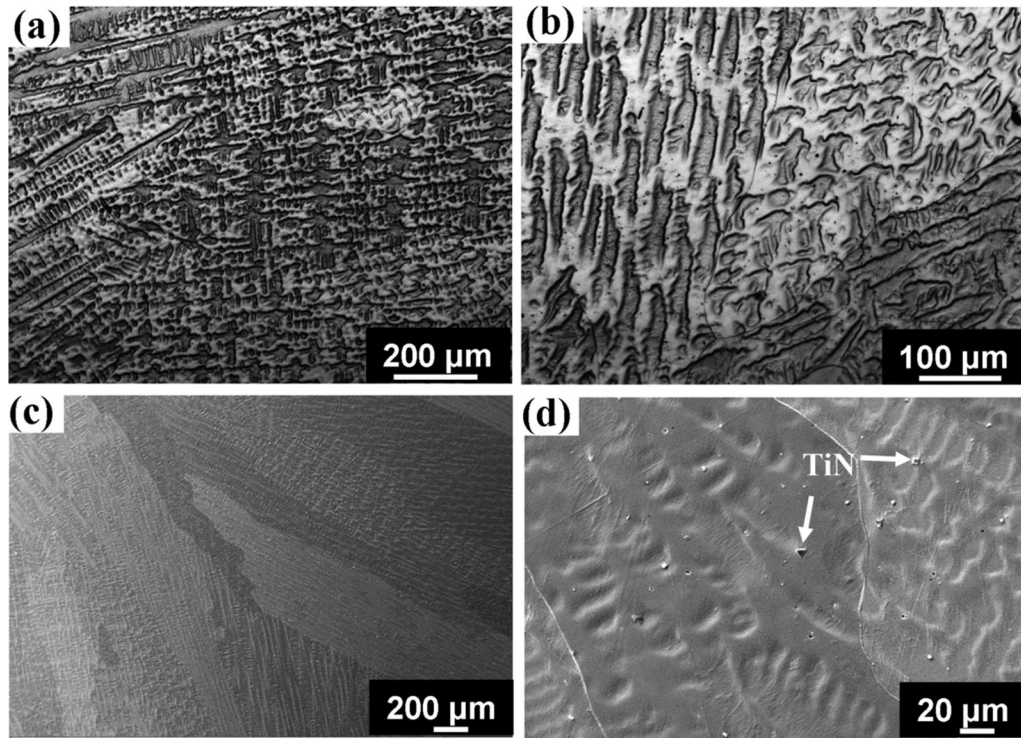


Fig. 3—(a, b) optical micrograph and (c, d) SEM micrographs of as-cast alloy at low and high magnification, respectively.

thermo-mechanical processing of the alloy in the single-phase γ region.

B. Microstructural Characterization

Figures 3(a) and (b) show the low and high magnification optical micrographs of the as-cast Ni–Fe–Co–Cr–Al alloy, respectively, exhibiting typical dendritic microstructure with an interdendritic spacing of $\sim 15 \mu\text{m}$.

The as-cast dendritic microstructure is further confirmed by the low and high magnification SE micrographs as depicted in Figures 3(c) and (d), respectively. Unlike our previous study, both the optical and SE micrographs confirm the absence of any as-cast L_{12} precipitates. Moreover, high magnification SE micrograph (Figure 3(d)) reveals a single-phase matrix with precipitation of TiN particles, which might have formed during melting and casting of the alloy due to the presence of some impurities in the mould or raw materials. It is observed that unlike our previous study, Co addition has suppressed the formation of as-cast γ' precipitates during solidification, as the high resolution SE micrographs also exhibits only single-phase as-cast microstructure with meagre amount of TiN precipitates.

Figures 4(a) and (b) show the SE micrographs of the alloy in homogenized and 73 pct cold-rolled conditions, respectively. The SE micrograph of the homogenized specimen (Figure 4(a)) clearly exhibits a fully recrystallized single-phase microstructure consisting of equiaxed grains of γ phase with average grain size of $\sim 58.3 \mu\text{m}$. The presence of TiN precipitates at some of the locations, along the grain boundaries as well as grain

interiors, is also evident (as indicated by white arrow marks in Figure 4(a)). Some TiN particles have been removed from the matrix during polishing, as indicated by black arrows. As expected, the heavy cold rolling led to deformed grains of γ matrix elongated in the rolling direction (Figure 4(b)). This heavily deformed cold-rolled specimen was annealed at 900°C with varying duration in the range of 20–1800 seconds to evaluate the static recrystallization behavior of the material.

The variation of microhardness as well as recrystallized fraction, as a function of isothermal holding time during annealing at 900°C , is shown in Figure 5(a). It is observed that the hardness value decreases with increase in isothermal holding time, which might be attributed to the formation of new strain-free recrystallized grains. The steady and slight decrease in hardness value is observed from 389 HV for cold-rolled condition to 375 and 361 HV during short annealing time of 20 and 60 seconds, respectively. Thereafter, it decreased considerably with the increase in annealing time up to 300 seconds. For the longer annealing duration of 900 seconds and more, there is insignificant variation in hardness, which signifies the completion of recrystallization. The recrystallized fraction of the annealed specimens was estimated by considering the microhardness values of the cold-rolled (CR) and cold-rolled and annealed (CR/Ann) specimens, which were obtained on the cross-sectional surface parallel to the rolling direction. The fraction recrystallized (X_{SRX}) is calculated using Eq. [1]:^[8,36]

$$X_{\text{SRX}} = (H_{\text{max}} - H_i)/(H_{\text{max}} - H_{\text{min}}), \quad [1]$$

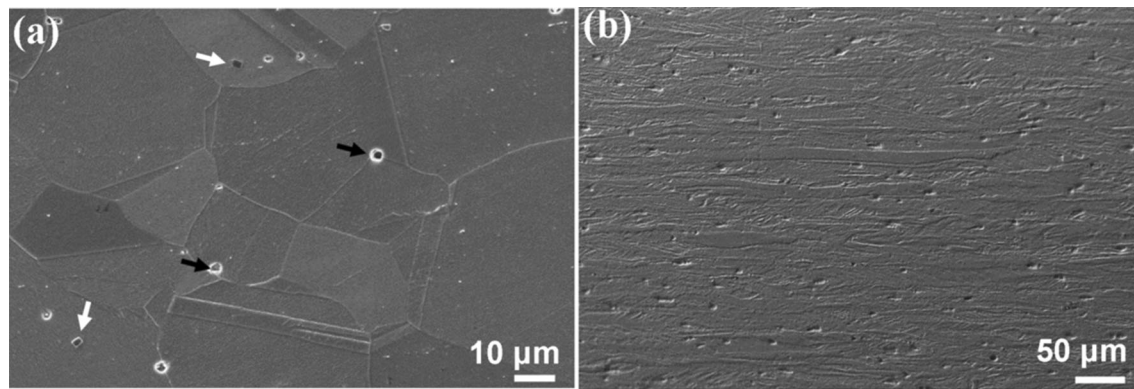


Fig. 4—SEM micrographs of designed alloy after (a) homogenization and (b) cold deformation of 73 pct.

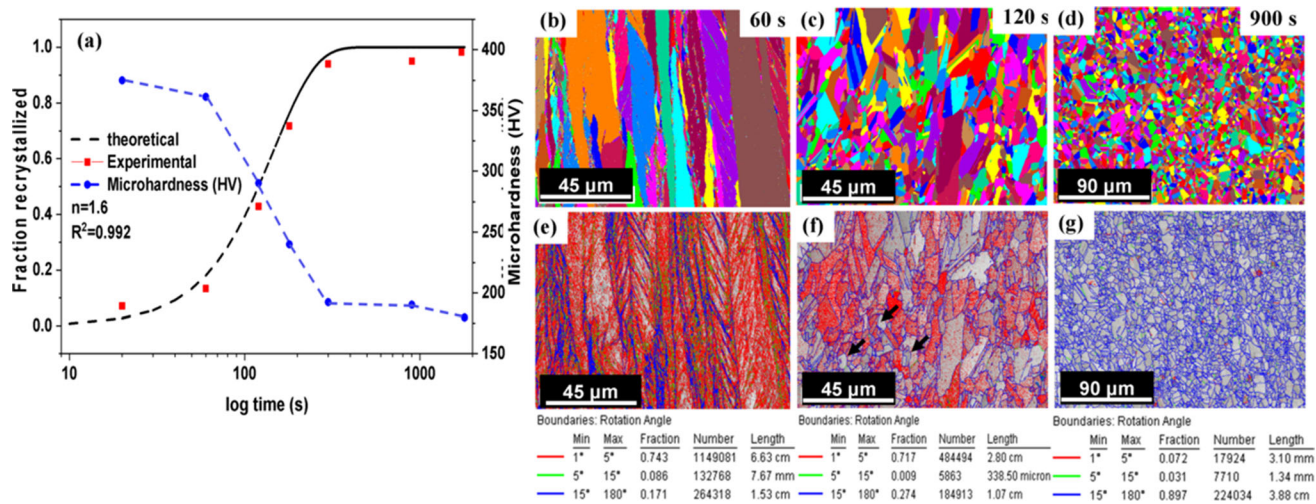


Fig. 5—(a) Fraction recrystallization and microhardness variation in the deformed specimen as a function of annealing time at 900 °C. Grain map and grain boundary plots, respectively, for cold-rolled specimens annealed at 900 °C for (b and e) 60 s (c and f) 120 s (d and g) 900 s.

where H_{max} , and H_{min} are maximum and minimum hardness observed in cold-rolled and fully recrystallized specimens, respectively. Here, H_i represents intermediate hardness values.

The experimentally estimated recrystallized fraction based on microhardness studies is plotted in Figure 5(a). In the same figure, the black coloured dashed-line represents the fitting curve on fraction recrystallized (X_{SRX}) based on the Avrami correlation, as given in Eq. [2].^[8]

$$X_{SRX} = 1 - \exp[-0.693(t/t_{0.5})^n], \quad [2]$$

where n , $t_{0.5}$ and t represent Avrami exponent, time required to complete 50 pct recrystallization and instantaneous time for recrystallization, respectively. The value of Avrami exponent (n) is assessed by fitting the Avrami equation with the experimentally estimated X_{SRX} values. The Avrami exponent for static recrystallization kinetics is estimated to be 1.6, which corroborates well with the data reported in literature.^[36,38,39] The analysis of softening curve clearly indicates that annealing duration of 900 seconds at 900 °C (CR/Ann-900 seconds) is sufficient to achieve almost

complete recrystallization. Hence, CR/Ann-900 seconds specimen was considered for ageing treatment. Figures 5(b) through (d) show the grain map of the cold-rolled specimens annealed at 900 °C for 60, 120 and 900 seconds, respectively. The evolution of a cold-rolled microstructure to almost fully recrystallized microstructure is evident from these micrographs. The grain map of the specimen annealed for 120 seconds exhibits both elongated and fine recrystallized grains. Figures 5(e) through (g), show the grain boundary distribution in each abovementioned conditions. It is observed that low angle grain boundaries (LAGBs) with misorientation < 15 deg are significantly high in the cold-rolled specimen annealed for short duration of 60 seconds (refer Figure 5(e)). The fraction of LAGBs decreased as the annealing duration increased from 60 to 120 seconds (Figure 5(f)). The presence of small strain-free recrystallized grains is observed in 120 seconds annealed specimen as marked by arrows in Figure 5(f). The prolonged annealing duration of 900 seconds results in a significant increase in the fraction of high angle grain boundary (HAGBs) with misorientation > 15 deg. A careful observation of

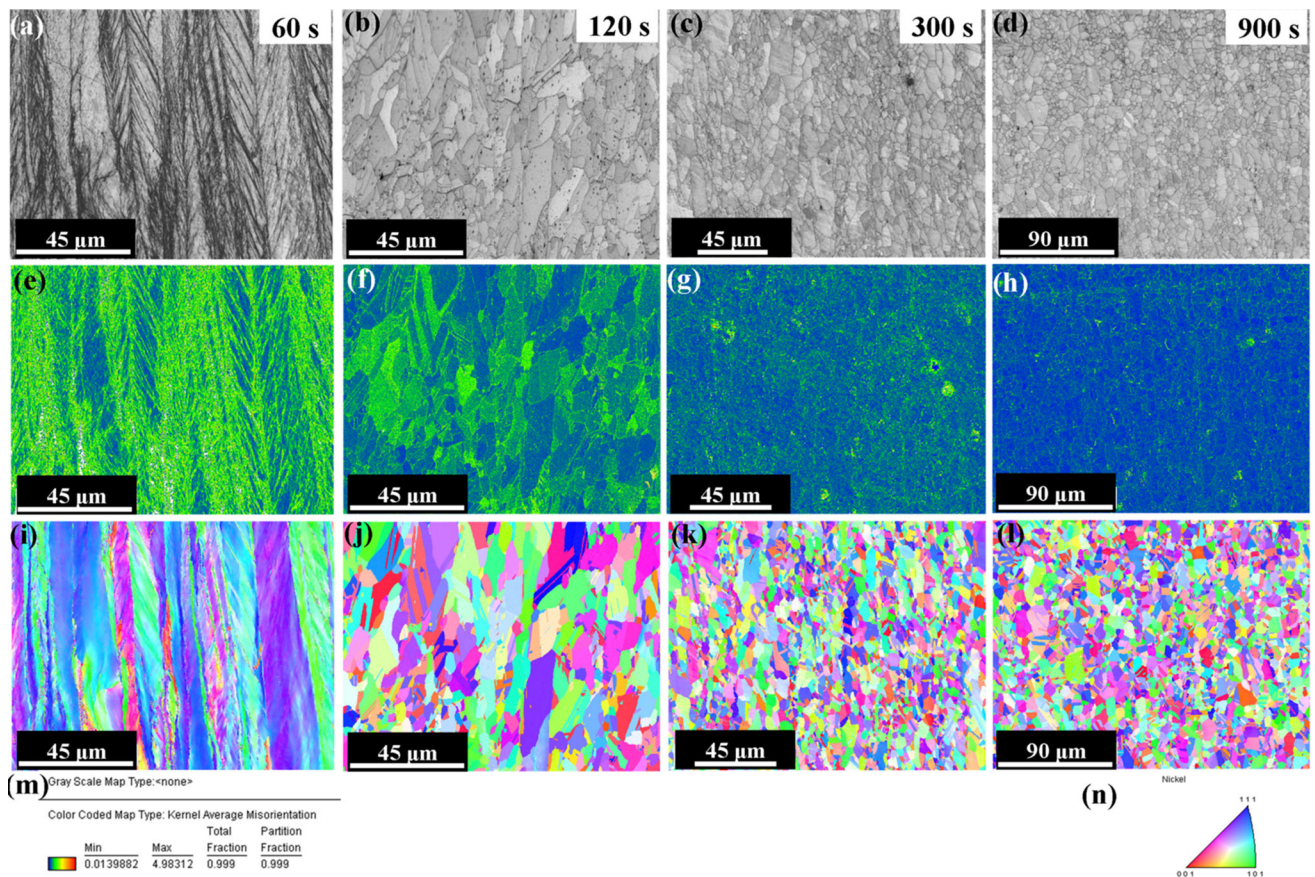


Fig. 6—(a to d) IQ maps (e to h) KAM maps and (i to l) IPF maps for specimens annealed at 900 °C for 60, 120, 300 and 900 s, respectively, (m) scale for KAM map (n) IPF figure for determination of orientation.

micrograph in Figure 5(g) exhibits ~ 0.9 fraction of HAGBs for 900 seconds annealed specimen, which is in good agreement with the estimated recrystallization fraction as shown in Figure 5(a).

The detailed microstructural characterization of the selected specimens annealed at 900 °C for varying duration, performed using EBSD technique, is further shown in Figure 6. It shows the EBSD micrographs of the specimens annealed at 900 °C for varying duration of 60, 120, 300 and 900 seconds. Figures 6(a) through (d) represent the image quality (IQ) maps for specimens annealed at 900 °C for 60 seconds (CR/Ann-60 seconds), 120 seconds (CR/Ann-120 seconds), 300 seconds (CR/Ann-300 seconds) and 900 seconds (CR/Ann-900 seconds), respectively.

It is observed that the cold-rolled specimen annealed for 60 seconds contains a highly deformed structure. These micrographs reveal the evolution of a highly deformed structure to small-grained recrystallized structures with increasing isothermal annealing duration. Further, the kernel average misorientation (KAM) map represented by Figures 6(e) through (h) for respective conditions reveal the evolution of a strain-free microstructure (in CR/Ann-900 seconds) from a highly strained initial microstructure (CR/Ann-60 seconds). The scale for the KAM map is shown in Figure 6(m), where it shows that the higher the KAM value on the

scale, the higher the dislocation density in the specimen. Figures 6(i) through (l) represent the inverse pole figure (IPF) maps for the specimens annealed for 60, 120, 300 and 900 seconds, respectively. As the specimen undergoes complete recrystallization, the system renders a random texture in the material.

The cold-rolled specimen annealed at 900 °C for 900 seconds was aged at 600 °C (CR/Ann-900 seconds / Ag-time) for varying duration of 3, 5 and 8 hours. A comparison of microhardness values of aged specimens (Figure 7(a)) reveals that hardness value increases with increase in ageing duration. This is possibly due to the formation of fine-sized precipitation of ordered γ' phase within the disordered FCC matrix of γ phase. Moreover, variation in microhardness is significantly low in case of the specimen aged for longer duration of 5 hours and more, which signifies the sluggish kinetics of γ' coarsening. This observation confirms that isothermal holding at 600 °C for 5 hours might be sufficient to introduce precipitation strengthening in the annealed specimens. In order to confirm the presence of γ' precipitates, XRD analysis of the as-cast specimen as well as specimens aged under various heat-treated conditions was performed (Figure 7(b)). The analysis of XRD peaks of all the studied specimens exhibits the presence of a single disordered FCC phase with estimated lattice parameter (a) of 0.357556 nm. The as-cast specimen exhibits a

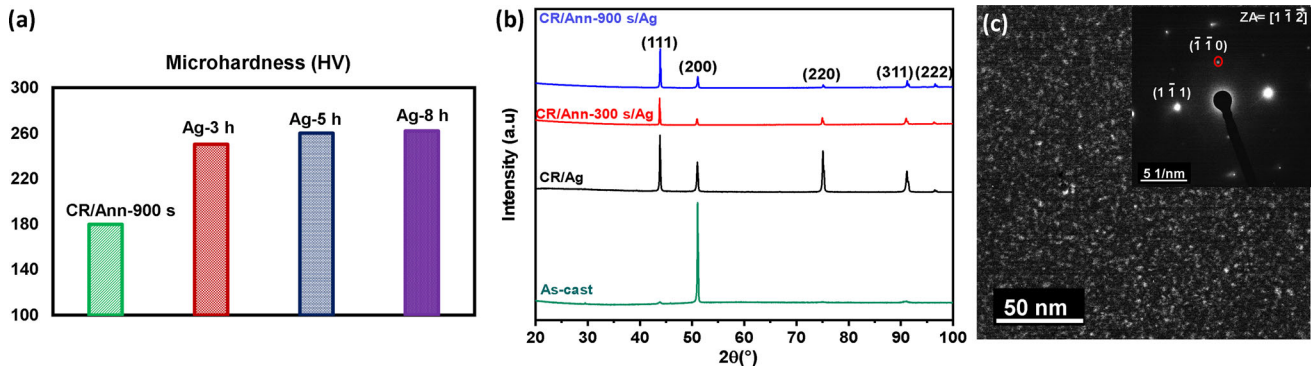


Fig. 7—(a) microhardness variation of CR/Ann-900 s specimen aged at 600 °C for 0, 3, 5 and 8 h, (b) XRD pattern of as-cast, CR/Ag, CR/Ann-300 s/Ag and CR/Ann-900 s/Ag specimens exhibiting a disordered FCC matrix, (c) TEM dark field image of CR/Ann-900 s/Ag specimen before tensile exhibiting homogeneous nanoprecipitation of $L1_2$ precipitates.

strong solidification texture along (200) plane whereas the annealed specimens exhibit random texture. Further, XRD analysis does not show any superlattice peaks of ordered γ' phase in the matrix, which might be due to low amount of extremely fine precipitates of γ' phase in the disordered γ matrix. Moreover, the transmission electron micrograph, as shown in Figure 7(c), exhibits extremely fine-sized γ' precipitates distributed homogeneously in the matrix for specimen CR/900 seconds/Ag-5 hours. It is clear that such fine-sized precipitates bear almost negligible misfit with the γ -matrix and hence are undetected in the XRD analysis.

C. Mechanical Property Evaluation

Based on the microhardness studies, as shown in Figure 7(a), an ageing schedule of 600 °C for 5 hours was selected for the evaluation of room temperature tensile properties. Hence, three specimens, namely (a) cold-rolled specimen (CR/Ag), (b) cold-rolled specimen annealed at 900 °C for 300 seconds (CR/Ann-300 seconds/Ag), and (c) cold-rolled specimen annealed at 900 °C for 900 seconds (CR/Ann-900 seconds/Ag), were aged based on the aforementioned ageing condition and evaluated for their tensile behaviour.

Figure 8(a) shows the stress-strain curve obtained from the aged specimens for the aforementioned three heat treatment conditions. The stress-strain curves show excellent strength-ductility synergy for all the studied conditions. The CR/Ag specimen shows a high strength of ~ 1275 MPa accompanied by an appreciable ductility of 40 pct. This high strength can be attributed to the highly deformed structure aided by significant precipitation hardening. Further, Co, Fe, and Cr are sources of solid solution strengthening in these specimens. The annealing for 300 seconds and subsequent ageing (CR/Ann-300 seconds/Ag) shows a significant reduction in strength value to 990 MPa compared to CR/Ag condition but a high ductility of ~ 60 pct. Similarly, 900 seconds annealing and ageing (CR/Ann-900 seconds/Ag) led to similar strength of 990 MPa but an increased ductility of ~ 67 pct. In comparison to CR/Ag specimen, both the CR/Ann-300 seconds/Ag and CR/Ann-900 seconds/Ag specimens demonstrate

comparable properties with decreased strength due to less dislocation hardening and high ductility due to ease in dislocation motion. The observed yield strength (σ_y), uniform tensile strength (σ_{UTS}) and total elongation (TE) is given in Table II.

Figures 8(b–c) and (d–e) show the fracture surfaces of the specimens for CR/Ag and CR/Ann-900 seconds/Ag conditions, respectively. The high ductility observed in both the specimens is corroborated by the formation of dimples across the fractured area, a signature of ductile fracture. Figure 9 shows the TEM micrographs of fractured CR/Ann-900 seconds/Ag specimen. Figures 9(a) and (b), show the bright and dark field micrographs, respectively, revealing annealing twins formed in the specimen during recrystallization. Figure 9(c) shows a homogeneous distribution of bulk nanoprecipitation of ordered $L1_2$ phase throughout the disordered FCC matrix, which gave rise to precipitation strengthening in the material. The size of the extremely fine precipitates varied in the range of 2 to 4 nm. The presence of deformation bands is revealed in the fractured specimen as shown in Figures 9(d) and (e), which represent the bright and dark field images, respectively, from the same location. The generation of GNDs and pile-up at the grain boundaries can be observed in Figure 9(f), which leads to strain hardening and thus high strength and ductility in the material.

IV. DISCUSSION

Conventional strengthening mechanisms operative in various alloy systems can be categorized as (a) solid solution strengthening, (b) precipitation strengthening, (c) dislocation strengthening, and (d) grain boundary strengthening. The engineered microstructure for high strength and ductility takes into account all the above strengthening mechanisms and manipulates their respective contribution to achieve an optimum combination of properties. The yield strength of a material is expressed as a function of all the above mentioned factors and is given by Eq. [3].^[3]

$$\sigma_y = \sigma_A + \Delta\sigma_S + \Delta\sigma_G + \Delta\sigma_D + \Delta\sigma_P, \quad [3]$$

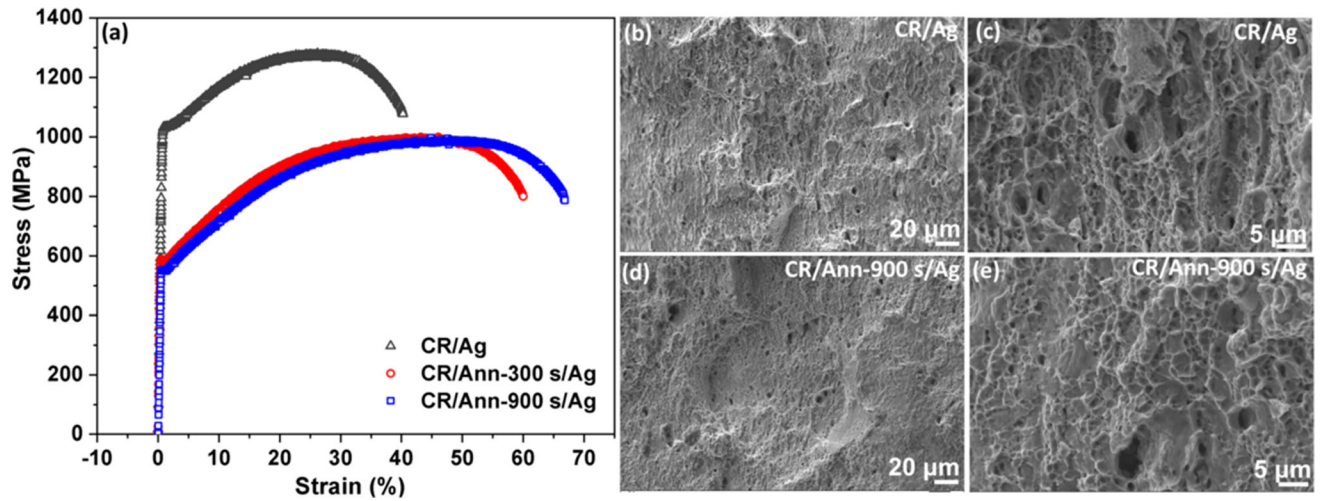


Fig. 8—(a) stress-strain curve for CR/Ag, CR/Ann-300 s/Ag and CR/Ann-900 s/Ag tensile test conditions (b, c) low and high magnification fracture surface of CR/Ag specimen and (d, e) low and high magnification fracture surface for CR/Ann-900 s/Ag condition, respectively.

Table II. Room Temperature Tensile Properties

Conditions	Yield Strength (σ_y)	Tensile Strength (σ_{UTS})	Total Elongation (Pct)
CR/Ag	1019	1275	40
CR/Ann-300 s/Ag	573	990	60
CR/Ann-900 s/Ag	529	990	67

σ_y and σ_{UTS} are in MPa.

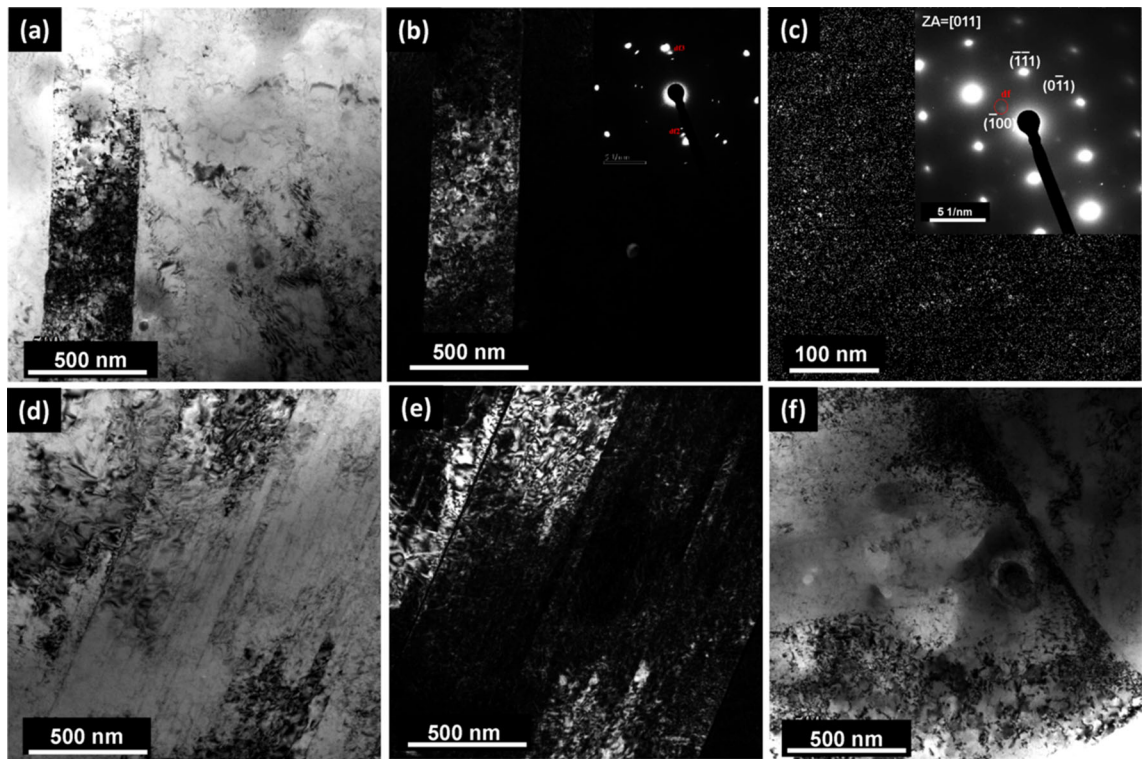


Fig. 9—(a) Bright field TEM micrograph showing annealing twins, (b) similar feature under dark field, (c) homogeneous nanoprecipitation of ordered L₁₂ precipitates (inset shows the selected area diffraction pattern), (d) Bright field micrograph showing deformation bands, (e) deformation bands under dark field, (f) dislocation accumulation at grain boundaries.

where σ_y is yield strength and σ_A is intrinsic strength of the material; $\Delta\sigma_S$, $\Delta\sigma_G$, $\Delta\sigma_D$ and $\Delta\sigma_P$ are the contributions due to solid solution strengthening, grain boundary strengthening, dislocation strengthening, and precipitation strengthening, respectively.

He *et al.*^[3] and Man *et al.*^[40] studied the effect of solid solution strengthening by considering the role of solute atoms like Al and Ti in concentrated NiFeCoCr solid solution systems and observed that its contribution is very low in comparison to other strengthening factors. In view of these observations, in the present MEA, the contribution of solid solution strengthening is expected to be lower. This is due to the fact that Al is the only possible solute in the studied Ni–Fe–Co–Cr-based system. As a result, the intrinsic strength (σ_A) and the contribution due to solid solution strengthening ($\Delta\sigma_S$) is combined together and the value of ($\sigma_A + \Delta\sigma_S$) is taken as $\sigma_B = 215$ MPa, which is the benchmark strength of Ni₂FeCoCr alloy in the work of Man *et al.*^[40] Therefore, the modified equation for σ_y becomes:

$$\sigma_y = \sigma_B + \Delta\sigma_G + \Delta\sigma_D + \Delta\sigma_P \quad [4]$$

The base strength for NiFeCoCr systems is 165 MPa.^[3,41] However, as the alloy in the present study has more Ni content, the benchmark strength is considered based on the study of Man *et al.*^[40] The other strengthening factors are calculated for each condition sequentially.

A. Dislocation strengthening ($\Delta\sigma_D$)

Dislocation hardening is a major strengthening factor in highly deformed materials, where the dislocation density becomes very high. In such deformed materials, dislocation mobility is impeded due to the strain fields of other dislocations resulting in high yield strength. The contribution of dislocation strengthening is calculated using the Bailey–Hersch relationship given in Eq. [5].^[42]

$$\Delta\sigma_D = M\alpha Gb\rho^{1/2}, \quad [5]$$

where M is Taylor's factor (3.06 for converting shear stress to normal stress in an FCC matrix), α is a material constant (~ 0.2 for FCC materials), b is the Burger's vector [$(\sqrt{2}/2) \times a = 0.254$ nm] and ρ is the dislocation density. The shear modulus (G) is taken as 78,500 MPa from literature data.^[3]

In the present study, the dislocation density (ρ) is calculated from the XRD data. The XRD peaks for the as-cast, CR/Ag and CR/Ann-300 seconds/Ag, and CR/Ann-900 seconds/Ag are shown in Figure 7(b). To calculate the dislocation density per unit area (ρ) for individual specimen, the modified Williamson–Hall (mW–H) method was adopted.^[43–45] The mW–H expression is given by References 43, 45, 46

$$\Delta K = (0.9/D) + (\pi M^2 b^2 / 2)^{1/2} \rho^{1/2} (K\bar{C}^{1/2}) + OK^2\bar{C}, \quad [6]$$

where D is the crystallite size (nm), M' is the Wilkens' parameter, \bar{C} is the average contrast factor, b and ρ have

the usual meaning as mentioned above, O is the coefficient of the higher order terms ($(\pi M^2 b^2 Q/2$, where Q is the correlation parameter) and $K = 2(\sin\theta)/\lambda$. Here, $\Delta K = \beta(\cos\theta)/\lambda$, where β is taken as full width half maxima (FWHM) from the XRD data (both β and θ are in radians) and λ is the wavelength in nanometers. The average contrast factor for each reflection is obtained from ANIZC software with $c_{11} = 238.3$, $c_{12} = 150.8$ and $c_{44} = 168.2$ for CoCrFeNi for $\{111\}\langle 110\rangle$ slip systems.^[47,48] Coefficients of $K\bar{C}^{1/2}$ and $K^2\bar{C}$ (0.9/D) term can be obtained by fitting a quadratic polynomial in the ΔK vs $K\bar{C}^{1/2}$ plot. As the main purpose of this fit is to obtain the ρ , the value of coefficient of $K\bar{C}^{1/2}$ is of interest. The exact value of ρ depends on the precise measurement of parameter M' that depends on the decay of the tails of the XRD line profiles. There is still no consensus in scientific literature on the exact value of Wilkens' parameter (M'), which depends on the outer cut-off radius (R_c) of the dislocations in the Wilken's dislocation distribution and the dislocation density (ρ)^[43,45] and its exact determination requires asymptotic Fourier analysis of the intensity distribution.^[49] However, the determination of M' through Fourier analysis is beyond the scope of the present investigation. Hence the values of M' have been obtained from literature. HajyAkbari *et al.*^[43] combined the mW–H and modern Warren Averbach (mW–A) method to calculate the dislocation density in lath martensitic steels, where the value of M' was calculated to be 1.4. Thirathipviwat *et al.*^[50] calculated the dislocation density in CoCrFeMnNi HEA using convolution multiple whole profile (CMWP) method and M' value varied from 1.32 to 0.21 for the cold swaged HEA. Similar range of 1.29–0.32 was obtained in works of Woo *et al.*^[45] for cold wrought CoCrNi MEA. Their work adopted both mW–H and mW–A analysis for accurate determination of ρ . The average value of M' obtained in their study was 0.57 for cold wrought CoCrNi MEA. In the present work, therefore, the value of Wilkens' parameter (M') is taken as 0.57.

Figures 10(a) through (c) show the variation of ΔK with respect to K by adopting the conventional W–H method for dislocation density determination for CR/Ag, CR/Ann-300 seconds/Ag, and CR/Ann-900 seconds/Ag conditions, respectively. The results show a non-monotonic increase in FWHM values with increasing K hinting at strain anisotropy in the material due to linear or surface defects. Figures 10(d) through (f) show the mW–H plots for CR/Ag, CR/Ann-300 seconds/Ag, and CR/Ann-900 seconds/Ag conditions, respectively, where the ordinate is ΔK but abscissa is changed to $K\bar{C}^{1/2}$ to consider the strain anisotropy effect. The plot shows better fit compared to the conventional W–H method but the R^2 values for each fit required further improvement. Hence, another parameter β' is introduced to consider the planar fault probability along with $W(g)$, which is the contrast factor for planar faults for each diffraction vector.^[51] $W(g)$ values are obtained from the work of Ungar *et al.*^[51] Thus Eq. [6] is modified to Eq. [7] as^[51]

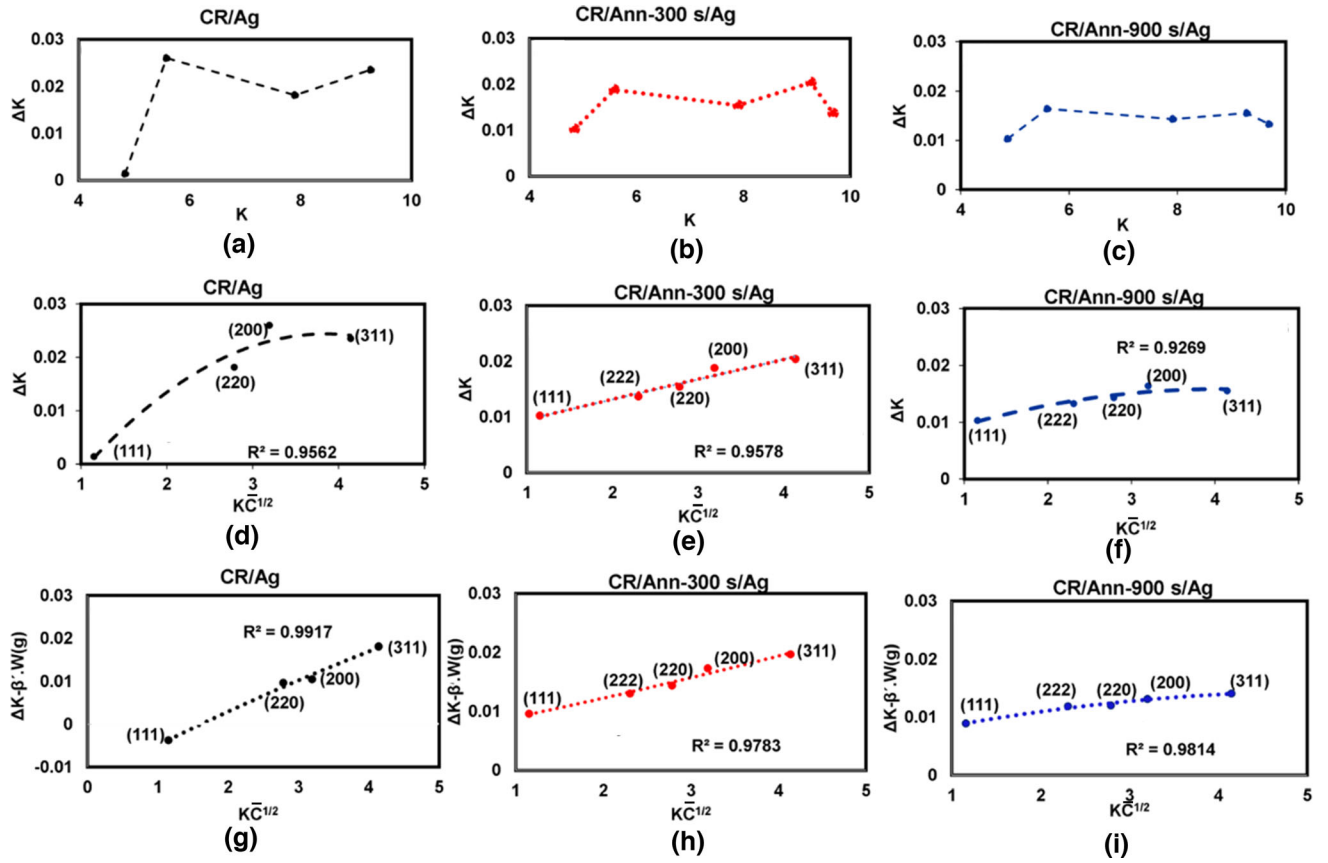


Fig. 10—(a to c) conventional W–H plot, (d to f) mW–H plot and (g to i) mW–H plot considering fault probability in the observed diffraction for CR/Ag, CR/Ann-300 s/Ag and CR/Ann-900 s/Ag conditions, respectively.

$$\Delta K - \beta' W(g) = (0.9/D) + (\pi M^2 b^2 / 2)^{1/2} \rho^{1/2} (K \bar{C}^{-1/2}) + O K^2 \bar{C} \quad [7]$$

The average contrast factor is taken as pure screw dislocations, which showed the best fit for the observed FWHM values. The average contrast factor for pure screw $\bar{C}_{\text{screw}}^{-1/2}$, $W(g)$, diffraction vector g , β' and resultant dislocation density is given in Table III. This modification gives a better fit with $R^2 > 0.96$ in all cases (refer Figures 10(g) through (i)). The dislocation densities for CR/Ag, CR/Ann-300 seconds/Ag, and CR/Ann-900 seconds/Ag are calculated to be $2 \times 10^{15}/\text{m}^2$, $6.5 \times 10^{13}/\text{m}^2$ and $4.1 \times 10^{13}/\text{m}^2$, respectively. As expected, estimated dislocation density is almost two order higher in cold-rolled specimen (CR/Ag) than cold-rolled and annealed specimens (CR/Ann-300 seconds/Ag), and CR/Ann-900 seconds/Ag). It is also noted that cold-rolled specimens annealed for varying duration of 300 and 900 seconds exhibit close values of dislocation density. Putting the values of ρ_1 , ρ_2 , and ρ_3 in Eq. [5], the strengthening contribution of dislocation density ($\Delta\sigma_D$) for the conditions CR/Ag, CR/Ann-300 seconds/Ag, and CR/Ann-900 seconds/Ag is 578, 98 and 78 MPa, respectively.

B. Precipitation Strengthening ($\Delta\sigma_P$)

As is evident from Figure 9(c), present alloy is nano-precipitation hardened with $L1_2$ precipitates, which nucleate homogeneously throughout the matrix. Moreover, considering the extremely fine size of precipitates and experimental limitations to accurately estimate the exact volume fraction of precipitates, equilibrium volume fraction of precipitates at the ageing temperature, as predicted by CALPHAD, was used for further calculations (0.33 for all conditions).

Considering the very fine size of precipitates, interaction of dislocation-precipitates resulting in Orowan looping is ruled out and particle shearing is expected to be the dominant strengthening mechanism. Therefore, two contributing factors can be considered (a) coherency strengthening ($\Delta\sigma_c$), and (b) modulus mismatch strengthening ($\Delta\sigma_M$), and their individual contributions can be calculated using the following relations.^[3]

$$\Delta\sigma_C = M\alpha_\epsilon (G\epsilon)^{3/2} (rf / 0.5Gb)^{1/2} \quad [8]$$

$$\Delta\sigma_M = 0.0055.M(\Delta G)^{3/2} (2f/G)^{1/2} (r/b)^{(3m/2)-1}, \quad [9]$$

where $M = 3.06$, $\alpha_\epsilon = 2.6$ is a constant for FCC structure, $m = 0.85$, $\epsilon = (2/3)$. ($\Delta a/a$) (where a is the lattice parameter of γ phase and Δa is the lattice mismatch between γ' precipitates and γ phase), G and b

Table III. Analysis of XRD Pattern

g	\bar{C}_{screw}	\bar{C}_{edge}	W(g) ^[51]	$K\bar{C}^{1/2}_{\text{CR/Ag}}$	$K\bar{C}^{1/2}_{\text{CR/Ann-300 s/Ag}}$	$K\bar{C}^{1/2}_{\text{CR/Ann-900 s/Ag}}$
				$\beta' = 0.002$	$\beta' = 0.0015$	$\beta' = 0.0009$
(111)	0.0566674	0.133362	0.43	1.1516	1.1526	1.1583
(200)	0.326793	0.30574	1	3.1926	3.1927	3.2015
(220)	0.124199	0.176456	0.71	2.785	2.785	2.7903
(311)	0.199541	0.224532	0.45	4.1394	4.138	4.146
(222)	0.0566674	0.133362	0.43	—	2.304	2.308

Table IV. Sources of Strengthening

Conditions	$\Delta\sigma_D$	$\Delta\sigma_P = \Delta\sigma_C + \Delta\sigma_M$	$\Delta\sigma_G$	Base Strength	σ_y (Predicted) (MPa)	σ_y (Exp.) (MPa)
CR/Ag	578	152	—	215	945	1019
CR/Ann-300 s/Ag	98	152	46	215	511	573
CR/Ann-900 s/Ag	78	152	36	215	481	529

are the shear modulus and Burger’s vector, respectively as mentioned in Section IV–A, r is the radius of the precipitates, f = equilibrium volume fraction of precipitates as predicted by CALPHAD (0.33 in the present case). Due to extremely small size rendering highly coherent boundaries and low volume fraction of precipitates, no superlattice peaks were observed in XRD analysis of aged specimens (refer Figure 7(b)). Hence, lattice misfit was calculated between the theoretical lattice parameter of pure Ni₃Al and that of the as-cast alloy. The lattice parameter of the disordered γ phase of the designed alloy was found to be $a = 0.3575$ nm which results in $\Delta a = 0.001$.^[52] The value of ΔG is obtained as the difference between shear modulus of precipitates and matrix (81.0–78.9) = 2.1 GPa).^[3,53] The radius of the precipitates was estimated through TEM and was found to be ~ 3 nm. Putting these values in Eqs. [8] and [9], corresponding coherency strengthening ($\Delta\sigma_C$) and modulus mismatch strengthening ($\Delta\sigma_M$) for all the studied conditions were estimated as 140 and 12 MPa, respectively.

C. Grain Boundary Strengthening ($\Delta\sigma_G$)

The dependence of grain boundary strengthening on the grain size of the material is given by the classical Hall–Petch relationship.^[3,54]

$$\sigma_{y,g} = \sigma_0 + k_y/d^{1/2}, \quad [10]$$

where $\sigma_{y,g}$ is the yield strength due to grain boundary strengthening, σ_0 is the intrinsic strength of the alloy, k_y is the strengthening or Hall–Petch coefficient (taken as 227 HV. $\mu\text{m}^{1/2}$)^[54] and d is the average grain diameter in micrometer.^[54] For CR/Ag condition, the grains are not equiaxed and maintain an aspect ratio (length/width of grains) significantly greater than one ($\gg 1$). As the boundaries are not clear in heavily deformed cold-rolled conditions, $\Delta\sigma_G$ is calculated for CR/

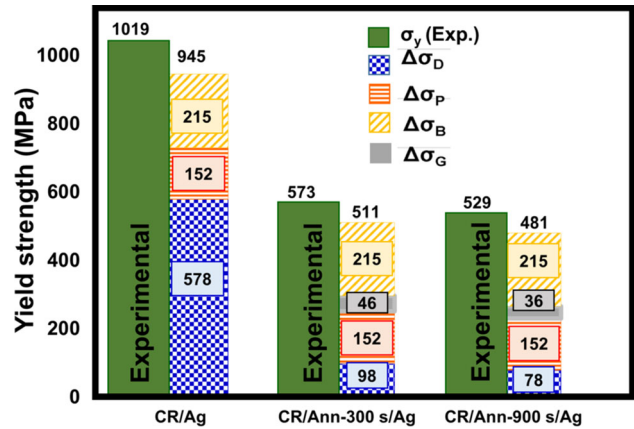


Fig. 11—Chart exhibiting contribution of various strengthening factors (Exp. represents the experimentally obtained values of the yield strength).

Ann-300 seconds/Ag and CR/Ann-900 seconds/Ag using Eq. [11]

$$\Delta\sigma_G = k_y(d^{-1/2} - d_H^{-1/2}), \quad [11]$$

where d_H is the diameter of the homogenized specimen, which was measured as 58.3 μm (refer Figure 4(a)). Putting $d = 9 \mu\text{m}$ for CR/Ann-300 seconds/Ag and $d = 12 \mu\text{m}$ for CR/Ann-900 seconds/Ag in Eq. [11] (refer Figures 6(c) and (d), respectively), the contribution of grain boundary strengthening is estimated as 46 and 36 MPa, respectively. Table IV represents the estimated individual contribution of all the strengthening sources along with predicted yield strength of all the selected aged specimens.

Figure 11 shows a comparison of experimentally obtained yield strength with that of empirically estimated yield strength by considering the contribution of various sources of strengthening. It is evident that for

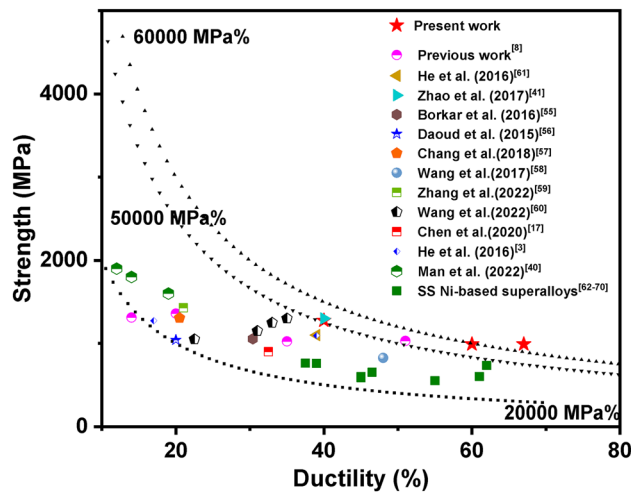


Fig. 12—Comparison of obtained room temperature mechanical properties with literature data.

CR/Ag condition the contribution of $\Delta\sigma_D$ is highest. The contribution of $\Delta\sigma_G$ is not significant in all cases but shows a slightly higher value for CR/Ann-300 seconds/Ag condition compared to CR/Ann-900 seconds/Ag condition. This might be attributed to the fact that there is not much grain refinement, which is prime factor in grain boundary strengthening. The bar chart clearly demonstrates the reasonably good agreement between experimentally obtained and empirically estimated yield strength (based on Eq. [4]) values. The difference in experimental and estimated yield strength values is mainly due to the uncertainties involved in estimation of many parameters and experimental data. This discrepancy can be attributed to the assumed values for G , M' , lattice misfit, *etc.*, which are obtained from the already published works and for slightly different compositions. Moreover, the size of precipitates is averaged out to be ~ 3 nm and the volume fraction is obtained from CALPHAD data which predicts the equilibrium amount of precipitates along with other phases including an ordered BCC-B2 phase. However, formation of BCC_B2 phase in the disordered FCC matrix is generally not realized owing to extremely sluggish kinetics of the studied alloy system (refer Figure 8). The contribution of precipitation hardening is thus kept constant based on average precipitate size, predicted equilibrium volume fraction and literature-based lattice misfit. The current study exhibits slightly lower values for the estimated yield strength (σ_y) compared to experimentally obtained yield strength. Nevertheless, this analysis is extremely helpful in gaining better insight into the contributions of various strengthening mechanisms to overall strength of the material.

Figure 12 shows the strength-ductility synergy in the presently designed and processed alloy in comparison to various HESAs and solid solution (SS) strengthened superalloys studied by other researchers.^[3,8,17,26,40,55–61] Similar to our previous work,^[8] solid solution-strengthened Ni–Fe–Cr-based superalloys were chosen for comparison owing to low volume fraction of γ' precipitates.^[62–70] It is evident that the product of strength and

ductility is much higher in the present alloy compared to various existing HEAs and SS superalloys. The criteria for the design of the present alloy and its processing is given in authors' previous work.^[8] The CR/Ag specimen demonstrates the energy absorption value close to 50,000 MPa pct as it has high strength of 1275 MPa with an excellent ductility of 40 pct. This high strength is due to high dislocation density in the specimen as observed from above calculations (refer Table IV). In the authors' previous work a Ni-based MEA was designed without the addition of Co, which led to excellent strength-ductility combinations.^[8] In the present work, Co was added and the composition was restricted to keep a strict γ - γ' -based microstructure. It is known that the addition of Co leads to low stacking-fault energy (SFE) in the material that promotes deformation twinning when the material is subjected to strain. Furthermore, the addition of Co also leads to the formation of finer $L1_2$ precipitates with lower anti-phase boundary (APB) energy. This study considered Co in the designed alloy and the results show higher ductility at the cost of slightly reduced strength compared to our previous work under similar conditions.^[8,36,37] Further, Co addition also lowers the volume fraction of γ' precipitates due to sluggish kinetics in Co-added system, which leads to finer γ' precipitates.^[36] Similar trend is observed for CR/Ann-300 seconds/Ag and CR/Ann-900 seconds/Ag conditions, where excellent ductility has been obtained on a minor sacrifice of strength compared to our previous work (CR/Ann-300 seconds/Ag and CR/Ann-900 seconds/Ag exhibited a strength-ductility combination of 35,840 and 52,530 MPa pct, respectively). Moreover, the grain size distribution in recrystallized specimens is more uniform in Co-added specimen compared to without Co-added alloy. Therefore, similar to our previous work, heterogeneous microstructure was tailored in the specimen with partial recrystallization and precipitation hardening. The calculations of respective strengthening mechanisms shed a light on the role of dislocations, grain boundary and precipitate strengthening and how the microstructure modifications affect the overall yield strength of the material. This thorough evaluation is helpful to design a suitable heterogeneous microstructure that yields good combination of strength and ductility.

The promising properties observed in the current study can be explored further to thoroughly investigate the deformation mechanisms operating under the chosen process conditions. Further, these alloys can be a potential candidate for high-temperature applications based on the results that have been obtained in various HESAs with Ni–Fe–Co–Cr-based systems.^[21,56,59]

V. CONCLUSION

A Ni–Fe–Co–Cr–Al-based MEA was designed through the CALPHAD approach. The designed alloy was thermo-mechanically processed to introduce heterogeneity in the microstructure *via* inhomogeneous recrystallization. Room temperature mechanical properties

were investigated for the chosen conditions. The contribution of various strengthening mechanisms was empirically estimated for each process condition. The salient conclusions drawn from the present study are as follows:

- (a) The designed alloy exhibits a γ - γ' -based microstructure with suppression of various undesired topologically closed packed (TCP) phases. The CALPHAD predicted BCC_B2 phase was not observed in the studied temperature range.
- (b) The recrystallization kinetics was studied for the designed alloy and the Avrami coefficient is estimated to be 1.6, which is close to those obtained for traditional superalloys and various HEAs.
- (c) The alloy showed excellent room temperature mechanical properties (~ 60,000 MPa pct) that supersede the strength-ductility synergy exhibited by various other Ni-based superalloys, heterogeneous MEAs and HEAs. Hence, alloy can be explored further at elevated temperatures to assess its potential at challenging superalloys for high-temperature applications.
- (d) The high dislocation density for CR/Ag condition rendered high strength (1019 MPa) with good ductility (40 pct). The estimated values of dislocation strengthening were comparable for CR/300 seconds/Ag (98 MPa) and CR/900 seconds/Ag (78 MPa) process conditions. The grain boundary strengthening was calculated for CR/300 seconds/Ag (46 MPa) and CR/900 seconds/Ag (36 MPa) specimens, where the former showed slightly higher value owing to finer grain size.
- (e) Empirically estimated yield strength corroborates well with the experimentally obtained yield strength in spite of many uncertainties in the estimated parameters.

ACKNOWLEDGMENTS

The authors are thankful to the Director, CSIR-National Metallurgical Laboratory, India, for providing the financial and equipment support to carry out this work. One of the authors, SK, would like to thank Dr. B. Mahato and Mr. P. S. Manoranjan Jena for extending their support in TEM investigation.

AUTHOR CONTRIBUTIONS

Shubhada Kar: Conceptualization, methodology, software, Writing-Original draft V. Shivam: Writing-Reviewing and Editing, V. C. Srivastava: Supervision, Writing- Reviewing and Editing, project administration, funding acquisition G. K. Mandal: Conceptualization, supervision, writing-Reviewing and editing, project administration, funding acquisition.

COMPETING INTERESTS

The authors declare that they have no known competing financial interests and personal relationships that could have appeared to influence the work reported in this paper.

REFERENCES

1. J.W. Yeh, S.K. Chen, S.J. Lin, J.Y. Gan, T.S. Chin, T.T. Shun, C.H. Tsau, and S.Y. Chang: *Adv. Eng. Mater.*, 2004, vol. 6, pp. 299–303.
2. B. Cantor, I.T.H. Chang, P. Knight, and A.J.B. Vincent: *Mater. Sci. Eng. A*, 2004, vol. 375–377, pp. 213–18.
3. J.Y. He, H. Wang, H.L. Huang, X.D. Xu, M.W. Chen, Y. Wu, X.J. Liu, T.G. Nieh, K. An, and Z.P. Lu: *Acta Mater.*, 2016, vol. 102, pp. 187–96.
4. J. Wang, H. Yang, H. Huang, J. Zou, S. Ji, and Z. Liu: *Mater. Sci. Eng. A*, 2020, <https://doi.org/10.1016/j.msea.2020.139974>.
5. Y.J. Liang, L. Wang, Y. Wen, B. Cheng, Q. Wu, T. Cao, Q. Xiao, Y. Xue, G. Sha, Y. Wang, Y. Ren, X. Li, L. Wang, F. Wang, and H. Cai: *Nat. Commun.*, 2018, vol. 9, pp. 1–8.
6. Q. Wang, T. Zhang, Z. Jiao, J. Wang, D. Zhao, G. Wu, J. Qiao, P.K. Liaw, and Z. Wang: *Mater. Sci. Eng. A*, 2023, vol. 873, 145036.
7. X. Feng, H. Yang, R. Fan, W. Zhang, F. Meng, B. Gan, and Y. Lu: *Mater. Sci. Eng. A*, 2020, <https://doi.org/10.1016/j.msea.2020.139591>.
8. S. Kar, V.C. Srivastava, and G.K. Mandal: *J. Alloys Compd.*, 2023, vol. 963, 171213.
9. C. Zhang, Q. Yu, Y.T. Tang, M. Xu, H. Wang, C. Zhu, J. Ell, S. Zhao, B.E. MacDonald, P. Cao, J.M. Schoenung, K.S. Vecchio, R.C. Reed, R.O. Ritchie, and E.J. Lavernia: *Acta Mater.*, 2023, vol. 242, 118449.
10. J.L. Yuan, Z. Wang, X. Jin, P.D. Han, and J.W. Qiao: *Mater. Sci. Eng. A*, 2022, vol. 853, 143712.
11. S. Il Baik, S.Y. Wang, P.K. Liaw, and D.C. Dunand: *Acta Mater.*, 2018, vol. 157, pp. 142–54.
12. J. Chen, X. Zhou, W. Wang, B. Liu, Y. Lv, W. Yang, D. Xu, and Y. Liu: *J. Alloys Compd.*, 2018, vol. 760, pp. 15–30.
13. D.B. Miracle, M.H. Tsai, O.N. Senkov, V. Soni, and R. Banerjee: *Ser. Mater.*, 2020, <https://doi.org/10.1016/j.scriptamat.2020.06.048>.
14. V. Soni, B. Gwalani, T. Alam, S. Dasari, Y. Zheng, O.N. Senkov, D. Miracle, and R. Banerjee: *Acta Mater.*, 2020, vol. 185, pp. 89–97.
15. O.N. Senkov, S.J. Kuhr, J.M. Shank, E.J. Payton, and C. Woodward: *Mater. Sci. Eng. A*, 2021, <https://doi.org/10.1016/j.msea.2021.141168>.
16. O.N. Senkov, D.B. Miracle, K.J. Chaput, and J.P. Couzinie: *J. Mater. Res.*, 2018, vol. 33, pp. 3092–3128.
17. Y.T. Chen, Y.J. Chang, H. Murakami, T. Sasaki, K. Hono, C.W. Li, K. Kakehi, J.W. Yeh, and A.C. Yeh: *Sci. Rep.*, 2020, vol. 10, pp. 1–11.
18. A. Yeh, T.K. Tsao, Y.J. Chang, K.C. Chang, J.W. Yeh, M.S. Chiou, S.R. Jian, C.M. Kuo, W.R. Wang, and H. Murakami: *Int. J. Metall. Mater. Eng.*, 2015, vol. 1, pp. 1–4.
19. T. Saito, A. Ishida, M. Yuyama, Y. Takata, K. Kawagishi, A.C. Yeh, and H. Murakami: *Crystals*, 2020, <https://doi.org/10.3390/cryst11010028>.
20. J.J. Yang, C.M. Kuo, P.T. Lin, H.C. Liu, C.Y. Huang, H.W. Yen, and C.W. Tsai: *J. Alloys Compd.*, 2020, vol. 825, 153983.
21. J. Joseph, M. Annasamy, S.R. Kada, P.D. Hodgson, M.R. Barnett, and D.M. Fabijanic: *Mater. Sci. Eng. A*, 2022, vol. 835, pp. 1–9.
22. T.K. Tsao, A.C. Yeh, and H. Murakami: *Metall. Mater. Trans. A*, 2017, vol. 48A, pp. 2435–42.
23. H.W. Luan, Y. Shao, J.F. Li, W.L. Mao, Z.D. Han, C. Shao, and K.F. Yao: *Ser. Mater.*, 2020, vol. 179, pp. 40–44.
24. O.N. Senkov, J.D. Miller, D.B. Miracle, and C. Woodward: *Nat. Commun.*, 2015, vol. 6, pp. 1–10.

25. W. Lu, X. Luo, B. Huang, P. Li, and Y. Yang: *Scr. Mater.*, 2022, vol. 212, pp. 8–13.
26. Y.L. Zhao, T. Yang, Y. Tong, J. Wang, J.H. Luan, Z.B. Jiao, D. Chen, Y. Yang, A. Hu, C.T. Liu, and J.J. Kai: *Acta Mater.*, 2017, vol. 138, pp. 72–82.
27. V. Shivam, S. Kar, G.K. Bansal, A.K. Chandan, B.K. Sahoo, G.K. Mandal, N.K. Mukhopadhyay, and V.C. Srivastava: *J. Alloys Compd.*, 2023, vol. 952, 170029.
28. A. Dash, A. Paul, S. Sen, S. Divinski, J. Kundin, I. Steinbach, B. Grabowski, and X. Zhang: *Annu. Rev. Mater. Res.*, 2022, vol. 52, pp. 383–409.
29. L. Wang, X. Wu, Y. Wu, G. Liu, Z. Han, Y. Zhang, Y. Su, S. Kang, J. Shen, and G. Zhang: *J. Mater. Sci. Technol.*, 2023, vol. 149, pp. 154–60.
30. H. Chen, X. Yuan, W. Ren, J. Peng, B. Ding, T. Zheng, J. Yu, P.K. Liaw, and Y. Zhong: *Mater. Res. Express*, 2020, vol. 7, p. 46507.
31. P.T. Lin, H.C. Liu, P.Y. Hsieh, C.Y. Wei, C.W. Tsai, Y.S. Sato, S.C. Chen, H.W. Yen, N.H. Lu, and C.H. Chen: *Mater. Des.*, 2020, <https://doi.org/10.1016/j.matdes.2020.109238>.
32. X.T. Fang, G.Z. He, C. Zheng, X.L. Ma, D. Kaoumi, Y.S. Li, and Y.T. Zhu: *Acta Mater.*, 2020, vol. 186, pp. 644–55.
33. S. Shin, C. Zhu, C. Zhang, and K.S. Vecchio: *Mater. Res. Lett.*, 2019, <https://doi.org/10.1080/21663831.2019.1652856>.
34. P. Sathiyamoorthi and H.S. Kim: *Prog. Mater. Sci.*, 2020, vol. 123, 100709.
35. S. Gorsse, Y.T. Chen, W.C. Hsu, H. Murakami, and A.C. Yeh: *Scr. Mater.*, 2021, vol. 193, pp. 147–52.
36. J.Y. Song, S. Sato, Y. Koizumi, and A. Chiba: *Adv. Mater. Res.*, 2014, vol. 922, pp. 711–15.
37. R.C. Reed: *The Superalloys Fundamentals and Applications*, vol. 9780521859, Cambridge University Press, Cambridge, 2006.
38. F. Masoumi, D. Shahriari, M. Jahazi, J. Cormier, and A. Devaux: *Sci. Rep.*, 2016, vol. 6, pp. 1–16.
39. Z. Yang, F. He, Q. Wu, K. Zhang, D. Cui, B. Guo, B. Han, J. Li, J. Wang, and Z. Wang: *Metall. Mater. Trans. A*, 2021, vol. 52A, pp. 3799–3810.
40. J. Man, B. Wu, G. Duan, L. Zhang, G. Wan, Y. Liu, and C. Esling: *Mater. Sci. Eng. A*, 2022, vol. 858, 144137.
41. Y.Y. Zhao and T.G. Nieh: *Intermetallics*, 2017, vol. 86, pp. 45–50.
42. Bailey: 1945, pp. 37–41.
43. F. HajyAkbar, J. Sietsma, A.J. Böttger, and M.J. Santofimia: *Mater. Sci. Eng. A*, 2015, vol. 639, pp. 208–18.
44. T. Ungár and A. Borbély: *Appl. Phys. Lett.*, 1996, vol. 69, pp. 3173–75.
45. W. Woo, Y.S. Kim, H.B. Chae, S.Y. Lee, J.S. Jeong, C.M. Lee, J.W. Won, Y.S. Na, T. Kawasaki, S. Harjo, and K. An: *Acta Mater.*, 2023, <https://doi.org/10.1016/j.actamat.2023.118699>.
46. E. Schafler, M. Zehetbauer, and T. Ungár: *Mater. Sci. Eng. A*, 2001, vol. 319–321, pp. 220–23.
47. J. Chakraborty, M. Ghosh, R. Ranjan, G. Das, D. Das, and S. Chandra: *Philos. Mag.*, 2013, vol. 93, pp. 4598–4616.
48. F. Tian, L.K. Varga, J. Shen, and L. Vitos: *Comput. Mater. Sci.*, 2016, vol. 111, pp. 350–58.
49. A. Borbély: *Scr. Mater.*, 2022, <https://doi.org/10.1016/j.scriptamat.2022.114768>.
50. P. Thirathipiwat, Y. Onuki, G. Song, J. Han, and S. Sato: *J. Alloys Compd.*, 2022, vol. 890, 161816.
51. T. Ungár, S. Ott, P.G. Sanders, A. Borbély, and J.R. Weertman: *Acta Mater.*, 1998, vol. 46, pp. 3693–99.
52. T.M. Pollock and A.S. Argon: *Acta Metall. Mater.*, 1992, vol. 40, pp. 1–30.
53. X. Luan, H. Qin, F. Liu, Z. Dai, Y. Yi, and Q. Li: *Crystals*, 2018, <https://doi.org/10.3390/cryst8080307>.
54. B. Gwalani, V. Soni, M. Lee, S.A. Mantri, Y. Ren, and R. Banerjee: *Mater. Des.*, 2017, vol. 121, pp. 254–60.
55. T. Borkar, B. Gwalani, D. Choudhuri, C.V. Mikler, C.J. Yannetta, X. Chen, R.V. Ramanujan, M.J. Styles, M.A. Gibson, and R. Banerjee: *Acta Mater.*, 2016, vol. 116, pp. 63–76.
56. H.M. Daoud, A.M. Manzoni, N. Wanderka, and U. Glatzel: *Jom*, 2015, vol. 67, pp. 2271–77.
57. Y.J. Chang and A.C. Yeh: *Mater. Chem. Phys.*, 2018, vol. 210, pp. 111–19.
58. Z.G. Wang, W. Zhou, L.M. Fu, J.F. Wang, R.C. Luo, X.C. Han, B. Chen, and X.D. Wang: *Mater. Sci. Eng. A*, 2017, vol. 696, pp. 503–10.
59. C. Zhang, Q. Yu, Y.T. Tang, M. Xu, H. Wang, C. Zhu, J. Ell, S. Zhao, B.E. MacDonald, P. Cao, J.M. Schoenung, K.S. Vecchio, R.C. Reed, R.O. Ritchie, and E.J. Lavernia: *Acta Mater.*, 2022, <https://doi.org/10.1016/j.actamat.2022.118449>.
60. C. Wang, C. Liang, M. Yang, C. Huang, Z. Yao, B. Qiu, K. Zhang, Y. Xie, M. Liang, W. Liu, J. Yang, and S. Zhou: *Mater. Des.*, 2022, vol. 221, 110940.
61. J.Y. He, H. Wang, Y. Wu, X.J. Liu, H.H. Mao, T.G. Nieh, and Z.P. Lu: *Intermetallics*, 2016, vol. 79, pp. 41–52.
62. INCOLOY alloy 803: www.specialmetals.com, Publication no. SMC-033. Copyright© Special Metals Corporation, 2004 (Sept 04).
63. INCOLOY DS: www.specialmetals.com, Publication no. SMC-097. Copyright© Special Metals Corporation, 2004 (Sept 2004).
64. INCOLOY alloy 832: www.specialmetals.com, Publication no. SMC-078. Copyright© Special Metals Corporation, 2003 (Oct 03).
65. INCOLOY alloy 600: www.specialmetals.com, Publication no. SMC-027. Copyright© Special Metals Corporation, 2008 (Sept 2008).
66. INCOLOY alloy 601: www.specialmetals.com, Publication no. SMC-028. Copyright© Special Metals Corporation, 2005 (Feb 05).
67. INCOLOY alloy 690: www.specialmetals.com, Publication no. SMC-079. Copyright© Special Metals Corporation, 2009 (Oct 09).
68. INCOLOY alloy 800: www.specialmetals.com, Publication no. SMC-047. Copyright© Special Metals Corporation, 2004 (Sept 04).
69. INCOLOY alloy 890: www.specialmetals.com, Publication no. SMC-089. Copyright© Special Metals Corporation, 2004 (Sept 04).
70. INCOLOY alloy 617: www.specialmetals.com, Publication no. SMC-029. Copyright© Special Metals Corporation, 2005 (Mar 05).

Publisher's Note Springer Nature remains neutral with regard to jurisdictional claims in published maps and institutional affiliations.

Springer Nature or its licensor (e.g. a society or other partner) holds exclusive rights to this article under a publishing agreement with the author(s) or other rightsholder(s); author self-archiving of the accepted manuscript version of this article is solely governed by the terms of such publishing agreement and applicable law.